Assessing the Ducting Phenomenon and its Potential Impact on GNSS Radio Occultation Refractivity Retrievals over the Northeast Pacific Ocean using Radiosondes and Global Reanalysis

Thomas E. Winning Jr. [1], Feiqin Xie[1] and Kevin J. Nelson[1,a]

[1] Texas A&M University – Corpus Christi, Corpus Christi, 78412, USA

[a] now at: Jet Propulsion Laboratory, California Institute of Technology, Pasadena, 91109, USA

Correspondence to: Thomas E. Winning Jr. (twinning@islander.tamucc.edu)

Abstract. In this study, high-resolution radiosondes from the MAGIC field campaign and ERA5 global reanalysis data are used to assess the elevated ducting layer characteristics along the transect over the northeastern Pacific Ocean from Los Angeles, California to Honolulu, Hawaii. The planetary boundary layer (PBL) height (PBLH) increases as the strength of the refractivity gradient decreases westward along the transect. The thickness of the prevailing ducting layer remains remarkably consistent (~110 m) in the radiosonde data. On the other hand, the ERA5 generally resolves the ducting features well, but underestimates the ducting height and strength especially over the trade cumulus region near Hawaii. A simple two-step end-to-end simulation is used to evaluate the impact of the elevated ducting layer on RO refractivity retrievals. A systematic negative refractivity bias (N-bias) below the ducting layer is observed throughout the transect, peaking (-5.42%) approximately 80 meters below the ~~PBL height~~PBLH, and gradually decreasing towards the surface (-0.5%). The N-bias shows strong positive correlation with the ducting strength. The ERA5 data underestimate the N-bias with the magnitude of the underestimation increasing westward along the transect.

1 Introduction

The troposphere, where most weather occurs, consists of two main layers: the planetary boundary layer (PBL) and the free atmosphere (FA) (Garratt, 1994). The PBL characteristics change frequently on both spatial and temporal scales and the PBL height (PBLH) can impact the exchange of heat, momentum, and particulate matter with the FA, making it a critical factor in global energy balances and water cycling (Stull 1988; Ramanathan et al. 1989; Klein and Hartmann 1993). Regular PBL observations are mainly limited to in situ measurements from surface stations and radiosondes. However, spatially and temporally dense in situ PBL observations are typically only available from field campaigns such as the Boundary Layer Experiment 1996 (BLX96, Stull et al. 1997), the Variability of the American Monsoon Systems (VAMOS) Ocean-Cloud-Atmosphere-Land Study Regional Experiment (VOCALS-REx, Wood et al. 2011), and the Marine Atmospheric Radiation Measurement (ARM) Global Energy and Water Experiment (GEWEX) Cloud System Studies (GCSS) Pacific Cross Section Intercomparison (GPCI) Investigation of Clouds (MAGIC, Zhou et al. 2015). Satellite observations of the PBL are also limited due to signal attenuation of the conventional infrared sounder in the lower troposphere and the low vertical resolution of microwave sounding instruments. Additionally, while the depth of the PBLH can vary from a couple hundred meters to a few kilometers (Ao et al. 2012; von Engeln and Teixeira 2013~~; Ao et al. 2012~~), the transition layer from the PBL to the FA is typically on the order of tens to hundreds of meters thick (Maddy and Barnet 2008), rendering ineffective PBL sensing from the low vertical resolution passive infrared and microwave sounders.

On the other hand, Global Navigation Satellite System (GNSS) radio occultation (RO) provides global atmospheric soundings with a vertical resolution of approximately 100 m in the lower troposphere under all weather conditions (~~Gorbunov et al., 2004;~~ Kursinski et al., 1997, 2000~~, 1997; Gorbunov et al., 2004~~). One of the major GNSS RO missions is the Formosat-3/Constellation Observing System for Meteorology, Ionosphere, and Climate (COSMIC), later referred to as COSMIC-1 (Anthes et al. 2008), and its follow-on mission COSMIC-2 (Schreiner et al. 2020). Numerous studies have documented the high value of GNSS RO for profiling the PBL and determining the PBLH (~~Nelson et al. 2021; Winning et al. 2017; Ho et al. 2015;~~ Ao et al. ~~2012;~~ ~~; Guo~~2008; Xie et al. ~~2011~~2008; Basha and Ratnam 2009; Guo et al. 2011; Ao et al. ~~2008; Xie et al. 2008~~2012; Ho et al. 2015; Winning et al. 2017; Nelson et al. 2021).

61 The advancement of the GNSS RO technique with open-loop tracking (Ao et al., 2003; Beyerle et

62 al., 2003; Sokolovskiy et al., 2006~~; Beyerle et al., 2003; Ao et al., 2003~~) along with the

63 implementation of ~~the~~ radio-holographic retrieval ~~algorithm (Jensen et al., 2004~~algorithms

64 (Gorbunov, 2002; Jensen et al., 2003; ~~Gorbunov, 2002~~Jensen et al., 2004) have led to much

65 improved PBL sounding quality. However, probing the marine PBL remains challenging as

66 systematic negative biases are frequently seen in RO refractivity retrievals (Xie et al. 2010; Feng

67 et al. 2020~~; Xie et al. 2010~~). One major cause of the refractivity bias (hereafter N-bias) is the RO

68 retrieval error due to elevated atmospheric ducting often seen near the PBLH (Sokolovskiy 2003;

69 Ao et al~~., 2007~~. 2003; Xie et al., 2006; Ao et al~~. 2003; Sokolovskiy 2003~~., 2007). This elevated

70 ducting prevails over the subtropical eastern oceans (~~Feng et al., 2020; Lopez, 2009;~~ von Englen

71 et al., 2003; Lopez, 2009; Feng et al., 2020), and the horizontal extent of ducting in these regions

72 can be on the order of thousands of kilometers (Xie et al. 2010; Winning et al. 2017~~; Xie et al.~~

73 ~~2010~~). In the presence of ducting, the vertical refractivity gradient exceeds the critical refraction

74 threshold for L-band frequencies (i.e., $dN/dz \le -157$ N-units km^{-1}). The steep negative refractivity

75 gradient is often observed in the vicinity of the PBLH, which is typically caused by an atmospheric

76 temperature inversion, a sharp decrease in moisture, or a combination of both. When ducting is

77 present, the Abel inversion (e.g., Fjeldbo et al., 1971) in the standard RO retrieval process

78 encounters a non-unique inversion problem due to a singularity in the bending angle, resulting in

79 large, systematic underestimation of refractivity (N) below the ducting layer (~~Xie et al. 2006;~~ Ao

80 et al., 2003; Sokolovskiy, 2003; Xie et al. 2006). The large uncertainty in RO refractivity coupled

81 with the singularity in bending angle hinders assimilation of RO observations into numerical

82 weather models, resulting in discarding of a significant percentage of RO measurements inside the

83 PBL (Healy, 2001).

84 To comprehensively assess the potential impact of ducting on GNSS RO retrievals, we begin by

85 constructing a detailed ground truth of PBL ducting statistics. This is derived from an extensive

86 set of high-resolution radiosonde data over the northeastern Pacific Ocean, a region known for

87 prevailing ducting conditions. Subsequently, we conduct a simulation study using the radiosonde

88 data to evaluate the N-biases caused by varying ducting characteristics. Section 2 provides details

89 of the two data sets used for this study: high-resolution radiosondes over the northeastern Pacific

90 Ocean and the colocated ECMWF Reanalysis version 5 (ERA5, Hersbach et al. 2020) profiles.

91 Additionally, we discuss the ~~co-location~~colocation criteria and the detection method for ducting

layer and the corresponding PBLH. Section 3 presents the ducting statistics for key variables, such as ducting height, PBLH, minimum refractivity gradient, and sharpness parameter. The characteristics of ducting including the thickness and strength along the cross-section are also shown. Furthermore, we evaluate the ducting-induced N-bias in GNSS RO refractivity retrievals by carrying out a two-step end-to-end simulation. Section 4 summarizes the findings and discusses the direction of future research.

2   Data and methods

2.1 MAGIC radiosonde and colocated ERA5 data

A collection of high-resolution radiosondes from the Marine Atmospheric Radiation Measurement (ARM) GCSS Pacific Cross Section Intercomparison (GPCI) Investigation of Clouds (MAGIC) are utilized as the primary data set in this analysis (~~Lewis 2016;~~ Zhou et al. 2015; Lewis 2016). The MAGIC field campaign took place from 26 September 2012 to 2 October 2013 as part of the U.S Department of Energy ARM Program Mobile Facility 2 (AMF2) aboard the Horizon Lines container ship, *Spirit*, which completed 20 round trip passes between Los Angeles, California and Honolulu, Hawaii during the yearlong data collection period (Painemal et al., 2015; Zhou, 2015). During each transit, radiosondes were launched at 6-hour intervals from the beginning of the program through the end of June 2013; the observation frequency increased to every 3 hours from July 2013 through the end of the campaign (Zhou et al., 2015). A total of 583 MAGIC radiosonde profiles were collected during the field campaign (Zhou et al., 2015), all with a vertical sampling frequency of 0.5 Hz (2 seconds), which provides an average vertical resolution of ~8 m below 3 km, but varies due to local vertical motion.

Use of this data set serves multiple benefits. First, the northeast Pacific transitions from a shallow stratocumulus-topped PBL to a higher, trade-cumulus boundary layer regime along the GPCI transect (Garratt, 1994). Second, the large number of observations over a 12-month time frame provides high temporal (diurnal and seasonal) and spatial profiling of the PBL along the GPCI transect seen in Fig.1. Finally, ducting is prevalent throughout the domain over which ~~creates~~the observations were captured creating an opportunity to perform an analysis over a natural cross-section of ~~refractivity field in~~ X (zonal) and Z (vertical) dimensions.
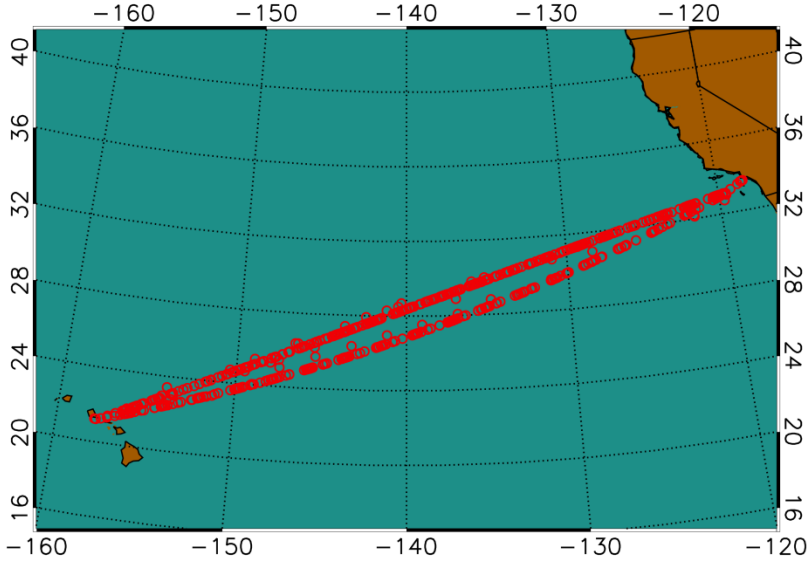
Figure 1: Location of radiosonde observations from the MAGIC field campaign October 2012–September 2013.

The radiosonde profiles are colocated with ERA5 model ~~reanalysis~~ profiles. The ERA5 ~~reanalysis~~ data have a horizontal grid resolution of 0.25°x0.25°, 1-hour temporal resolution, and 137 ~~uneven~~non-linear vertical model levels from the surface to 0.01 hPa. The model level density decreases with height: on average, there are 19 model levels below 1 km (10 –100 m resolution), which reduces to 8 levels between 1 and 2 km (100 – 160 m resolution), and further reduces to 5 levels between 2 and 3 km (160-200 m resolution). Each MAGIC radiosonde profile was colocated with the nearest ERA5 grid point that is within 1.5 hours of the closest 3-hourly model ~~reanalysis~~ profile.

2.2 ~~PBL height~~PBLH detection with the minimum gradient method

At GNSS L-band frequencies, the atmospheric refractivity (N in N-units) is derived from the refractive index n, where $N = (n - 1) \times 10^6$ and, in the neutral atmosphere (Kursinski et al., 1997), is a function of the atmospheric pressure (P in mb), temperature (T in K), and partial pressure of water vapor (P_w in mb) as seen in Eq. (1) from Smith and Weintraub (1953).

$$N = 77.6 \frac{P}{T} + 3.73 \times 10^5 \frac{P_w}{T^2}, \tag{1}$$

Over the subtropical eastern oceans, a sharp decrease in moisture is often associated with a strong temperature inversion marking a clear transition from the PBL to the FA. Both the distinct decrease in moisture and the temperature inversion lead to a sharp negative refractivity gradient which can be precisely detected from GNSS RO. Numerous studies have implemented the simple gradient

5

141 method to detect the PBLH, i.e., the height of the minimum refractivity gradient (~~Ao et al., 2012;~~

142 ~~Seidal et al., 2010; Xie et al., 2006). To assess the robustness of PBLH detection with gradient~~

143 ~~method, Ao et al. (2012) introduced the sharpness parameter ($\widetilde{N}'$) to measure the relative~~

144 ~~magnitude of the minimum gradient from surface to 5 km as follows:~~ Xie et al., 2006; Seidel et

145 al., 2010; Ao et al., 2012).

146 ~~$\widetilde{N}' \equiv -\dfrac{N^{t}_{min}}{N^{L}_{RMS}}$,~~ (2)

147 ~~Each refractivity gradient profile can then be filtered to identify the PBLH values with sharpness~~

148 ~~parameter exceeding a specific threshold, thus increasing the robustness of PBLH detection.~~ In

149 this study, the MAGIC radiosonde refractivity profiles were first interpolated to a uniform 10 m

150 vertical grid and then smoothed by a 100 m boxcar window to reduce the noise in the gradient

151 profile resulting from the high sampling rate. Moreover, the 100 m smoothed radiosonde will be

152 more consistent with the vertical resolution of GNSS RO measurements (e.g. Gorbunov et al.,

153 2004). Colocated ERA5 data were also vertically interpolated to the same 10 m grid but not

154 smoothed as these data do not contain the inherent noise as the radiosonde observations. ~~In~~

155 ~~addition~~In the case of both data sets, quadratic interpolation is used to translate the refractivity

156 profiles from their native height values to a uniform height. Finally, as the elevated ducting layer

157 is the focus of this study, the lowest 0.3 km above mean-sea-level of the N-profile ~~near surface~~ are

158 excluded (e.g., Xie et al., 2012). Subsequently, the height of the minimum refractivity gradient

159 (within 0.3 km and 5 km) will be identified as the PBLH.

160 **2.3 Ducting layers**

161 The refractivity gradient profile is calculated by differentiating the 10 m interpolated refractivity

162 profile with respect to height. When the vertical refractivity gradient is less than the critical

163 refraction (dN/dz ~~$\approx$~~$\leq$ −157.0 N-units km^{-1}), ducting occurs (Sokolovskiy, 2003). A ducting layer is

164 identified as any interval of continuous points with a vertical refractivity gradient equal to or less

165 than −157 N-units km^{-1}. Instances of multiple ducting layers occurring within a profile are present

166 for both the MAGIC (31.5%) and ERA5 (6.7%) data sets. In this study, we only recognize one

167 dominant "ducting layer" in each profile where the minimum vertical gradient is located. The

168 ducting layer thickness (Δh) is defined as the interval between the top and bottom of the ducting

169 layer where the refractivity gradients reach critical refraction. Similarly, the strength of each

170 ducting layer (ΔN) is defined as the refractivity difference between the bottom and top of the

171 ducting layer. The ducting layer height is ~~in reference to~~defined as the height of the top of the

172 ducting layer (Ao, 2007), which is ~~generally~~ slightly above the PBLH.

173 Figure 2 shows vertical profiles of refractivity (N-units ~~x 1/10, N~~/10), temperature (T), and specific

174 humidity (q) along with their respective vertical gradients (dN/dz, dT/dz, and dq/dz) from a

175 representative MAGIC radiosonde (Fig. 2a,b) case located at (23.~~69°N~~69°, −150.~~02°E~~02°), and its

176 colocated ERA5 (Fig. 2c,d) profile at (23.~~75°N~~75°, −150.~~00°E~~00°). The PBLH of the radiosonde

177 (2.10 km) is almost identical to the colocated ERA5 (2.14 km) and the "dominant" ducting layer

178 near the PBLH demonstrates similar thickness. However, a second, weaker ducting layer seen in

179 the radiosonde above the PBLH was not captured by the ERA5. Note that the weak gradients seen

180 above the minimum in the ERA5 refractivity gradient (Fig. 2d) are a result of the vertical derivative

181 being calculated from the interpolated ERA5 refractivity profile and do not appear for larger

182 interpolation intervals suggesting that the non-linearity of the ERA5 vertical grid at this height

183 affects the vertical gradient. These features of approximately 15 N-units km^{-1} magnitude are only

184 noticed in the plotting and do not impact the results of the study, as only the moisture-induced

185 minimum gradient values are large enough in magnitude to exceed the minimum gradient
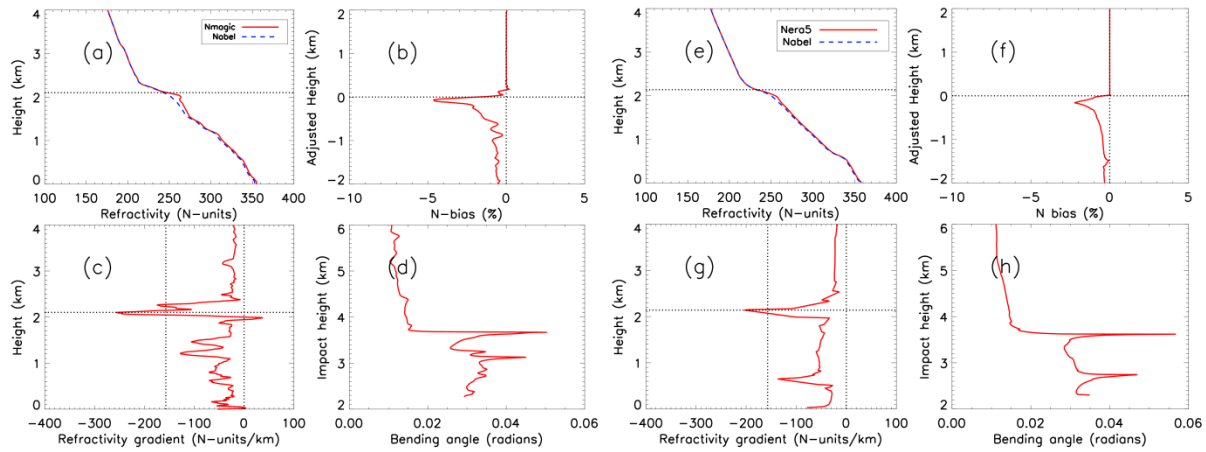
186 threshold.
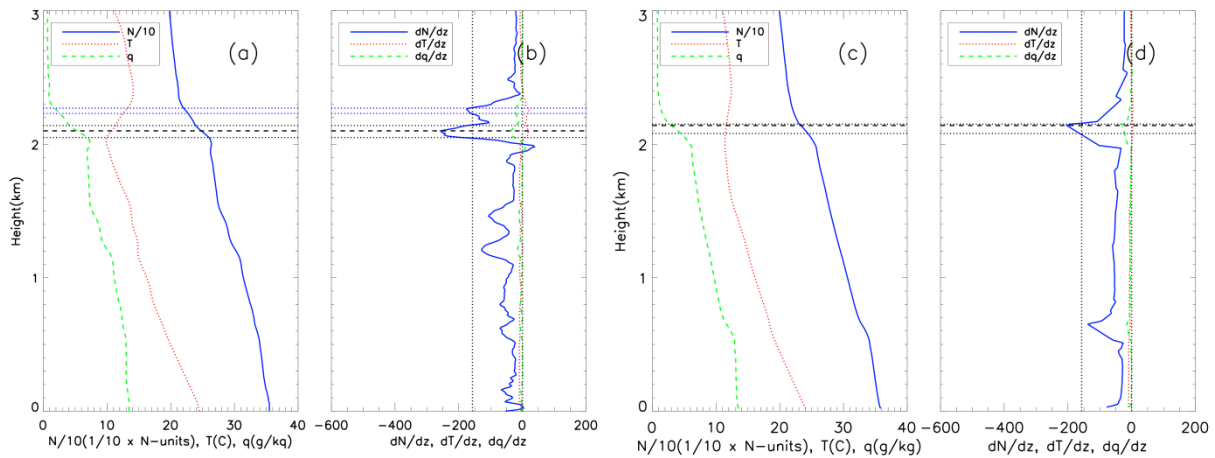
187

188 **Figure 2: Vertical profiles of refractivity (~~1/10 x N in~~ N-units, ~~N~~ /10, solid blue), temperature (T in °C, dotted red) and**
189 **specific humidity (q in g kg^{-1}, dashed green) for (a) radiosonde at (23.~~69°N~~69°, -150.~~02°E~~02°) launched at 2012-10-02, 05:30**
190 **UTC, and (c) colocated ERA5 at (23.~~75°N~~75°, -150.~~00°E~~00°); and associated gradient profiles for radiosonde (b) and ERA5**
191 **(d). The horizontal dashed line highlights the height of the minimum gradient, i.e., PBLH. The paired horizontal dotted**
192 **lines represent the bottom and top of the two ducting layers in the radiosonde profile (a and b) but only one in the ERA5**
193 **profile (c and d).**

194 ## 2.4 Evaluation of GNSS RO N-bias resulting from ducting

195   In order to estimate the systematic negative *N*-bias in GNSS RO observations in the presence of

196   ducting, we use an end-to-end simulation on the radiosonde and ERA5 refractivity profiles. The

197   simulation consists of a two-step process adapted from Xie et al. (2006). The first step is to

198   simulate the 1-dimensional GNSS RO bending angle as a function of impact parameter (i.e., the

199   product of refractive index and the radius of the Earth's curvature) by forward Abel integration of

200   an input refractivity profile assuming a spherically symmetric atmosphere (~~Sokolovskiy, 2001;~~

201   ~~Eshleman, 1973,~~ Fjeldbo and Eshleman, 1968; Eshleman, 1973; Sokolovskiy, 2001). The second

202   step is to simulate the GNSS RO refractivity retrieval by applying the Abel inversion on the

203   simulated bending angle from step one. In the absence of ducting, the impact parameter increases

204   monotonically with height, allowing a unique solution to the inverse Abel retrieval that is the same

205   as the original refractivity profile input. However, in the presence of an elevated ducting layer, the

206   Abel retrieval systematically underestimates the refractivity profile due to the non-unique Abel

207   inversion problem resulting from the singularity in bending angle across the ducting layer

208   (Sokolovskiy 2003; Xie et al., 2006~~; Sokolovskiy 2003~~). It should be noted that after the 100 m

209   vertical smoothing on radiosonde (no smoothing on ERA5) profiles as described in section 2.2, an

210   additional 50 m vertical smoothing has been applied to the simulated bending angle profiles of

211   both radiosonde and ERA5 data sets to alleviate the challenge of integration through the very sharp

212   bending angle resulting from ducting in the inverse Abel integration procedure (Feng et al., 2020).

213   Figure 3 shows the end-to-end simulation results for the same radiosonde (a–d) and the colocated

214   ERA5 (e–h) cases from Fig. 2. Figures 3a and 3e show refractivity profiles from the radiosonde

215   (~~N_{rds}~~N_{MAGIC}) and the colocated ERA5 (N_{ERA5}) data as well as their corresponding Abel refractivity

216   retrievals (N_{Abel}). ~~The~~The refractivity gradients are shown in Figures 3c and 3g. The derived PBLH

217   is marked by a horizontal dotted line. The peak bending ~~angle is~~angles in Figures 3d and 3h are

218   consistent with the sharp refractivity gradient. Figure 3b shows the fractional *N*-bias between the

219   simulated Abel retrieved RO refractivity profile and the ~~observation, i.e., ((N_{Abel} =~~

220   ~~N_{Obs})/N_{Obs}).~~radiosonde, whereas Figure 3f shows the same for the ERA5 profile. Considering the

221   significant spatial and temporal variations of ducting height along the transect, each *N*-bias profile

222   is ~~normalized to its~~displayed as a function of an adjusted height, which is the height minus the

223   corresponding PBLH for the purposes of ~~comparison~~profile intercomparison. For example, the

224   zero-adjusted height refers to the PBLH for each individual profile. The systematic negative *N*-

225   bias is ~~clearly~~ shown below the ducting layer marked by the PBLH in both cases, with the biases

226 decreasing at lower altitude, the largest magnitude bias (−5% for radiosonde; −2.5% for ERA5)

227 close to the ducting height and a minimum magnitude approaching zero near the surface.

228

3   Analysis

234 Quality control for radiosonde (and colocated ERA5) profiles was based on five key criteria. First,

235 a total of 19 radiosonde and 24 ERA5 profiles near the southern California coast were removed

236 due to their positions east of −~~120°E~~120° or anomalously high PBL (PBLH > 3.0 km) with no

237 distinct minimum gradient. The remaining profiles in the easternmost portion of the domain were

238 too few in number to calculate meaningful statistics. Second, any profile lacking critical refraction

239 (i.e. dN/dz < −157 N-units km^{-1}) points was excluded from the analysis which resulted in the

240 removal of 47 radiosonde and 176 ERA5 profiles. Third, the noisy bending angle could result in

241 errors in Abel refractivity retrieval and cause positive *N*-bias. Therefore, the profiles with *N*-bias

242 greater than +0.5% are excluded resulting in the removal of 61 MAGIC profiles and 16 ERA5

243 profiles. Fourth, the profiles with only surface ducting, i.e., below 300 m threshold, are discarded.

244 Finally, 25 radiosonde profiles and 2 ERA5 profiles were removed due to the Abel retrieval failure.

245 After implementing all quality control measures, the number of radiosonde and ERA5 profiles

246 used for the *N*-bias analysis is reduced to 396 and 319 profiles, respectively.

3.1 PBL analysis

248   To evaluate the ducting properties along the transect from the coast of southern California to

249   Hawaii, we group the MAGIC radiosonde and the colocated ERA5 profiles into eight 5˚ longitude

250   bins between −160.0˚ and −120.0˚, which allows for the spatial variation of the PBL, ducting layer

251   and the associated properties along the transect to be easily illustrated. Figure 4 shows the median

252   value of PBLH (a), minimum gradient (b) and sharpness parameter (c) along the transect. The

253   median-absolute-deviation (MAD) for each parameter is also shown.

254   In Fig. 4a, the MAGIC radiosondes (rds) clearly show the gradual increase of the PBLH along the

255   transect from the shallow stratocumulus-topped PBL (~800 m) near the southern California coast

256   westward to the much deeper trade-cumulus regime (~1.8 km) near Hawaii. A similar structure is

257   seen in the colocated ERA5 data but with an average low bias of 165 m below the radiosonde.

258   However, a nearly 800 m underestimation in PBLH over the two westernmost bins near Hawaii is

259   also seen, this is consistent with what is found over the equivalent trade cumulus region of the

260   subtropical southeast Pacific Ocean (Xie et al., 2012). Such a discrepancy could be due to the

261   sensitivity of the gradient method to the vertical resolution of the data. Over the western segment

262   of the transect (near Hawaii), two major gradient layers (one at ~1 km and the other at ~2 km) with

263   comparable refractivity gradients are often observed (e.g., Fig. 2). The gradient layer ~~at around~~near

264   2 km is well-known as the trade-wind inversion~~. While~~ (Riehl, 1979; Ao et al., 2012; Xie et al.,

265   2012), while the lower-level gradient layer at ~1 km, is generally called a mixing layer~~. Note~~ (Xie

266   et al., 2006). Due to the ~~radiosonde data exhibit consistent~~differences in vertical sampling ~~(~8 m~~

267   ~~resolution) below 3 km, and resolve both layers well. However, the ERA5 data have an uneven~~

268   ~~vertical sampling intervals increasing with height, with 10 – 100m resolution below~~ noted in

269   Section 2.~~1 km, 100 – 160 m within 1-2 km, and 160 – 200 m within 2-3 km. Therefore~~, the ERA5

270   data are more likely to resolve the sharp gradient structure below 1 km than the one at higher

271   altitude. This could result in resolving the mixing layer (below 1 km) with the sharpest refractivity

272   gradient, instead of the trade-wind inversion near 2 km in the ERA5 data. Note that the larger

273   median absolute deviation for the westernmost bins compared to the rest of the transect illustrates

274   the existence of greater PBLH variability closer to the trade-cumulus boundary layer regime. The

275   westward decreasing magnitude of the minimum refractivity gradient (Fig. 4b) and sharpness

276   parameter (Fig. 4c) indicates the westward weakening of moisture lapse rate and/or temperature

277   inversion across the PBL top, which is consistent with the decreasing synoptic-scale subsidence

278   from the California coast to Hawaii (Riehl, 1979).

279
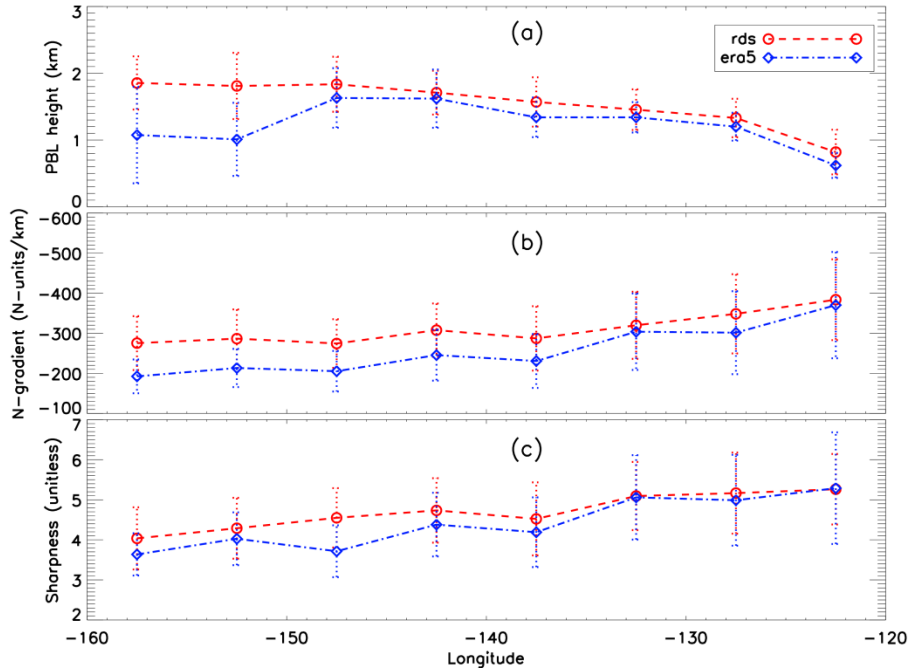
Figure 4: Zonal transect of 5° bin MAGIC and ERA5 PBLH (a), minimum refractivity gradient (b) and sharpness parameter (c) for MAGIC (median in red circle and dashed line, MAD in red dotted error bars) and ERA5 (median in blue diamond and dot-dashed line, MAD in blue dotted error bars).

It is also notable that the ERA5 systematically underestimates not only the PBLH but also the magnitude of the minimum gradient across the entire transect. This can also be seen in the sharpness parameter west of −132.5°. This discrepancy could be partially attributed to the decrease in vertical sampling in ERA5 profiles as compared to the radiosondes, the result of which leads to a weaker PBL refractivity gradient and coincides with an increasing PBLH. Therefore, the underestimation of the ERA5 minimum refractivity gradient increases in magnitude from east to west and becomes most prominent near Hawaii where the PBLH reaches the maximum height over the region.

**3.2 Ducting characteristics**

As introduced in Sect. 2.3, the key characteristics of the ducting layer along the transect will be investigated, these include the ducting layer height, thickness (Δh), and strength (ΔN), as well as the average refractivity gradient within the ducting layer ($\Delta N/\Delta h$). All parameters are interpolated to a 10 m vertical grid.

The ducting layer heights from both radiosonde and ERA5 show a westward increase along the transect is, as seen in Fig. 5a. Note again that the ERA5 shows a systematic ~100–200 m low bias

299   when compared to the radiosondes between −122.5˚ and −147.5˚, with the difference increasing

300   to more than 500 m near Hawaii. The ducting layer thickness is the median height from the bottom

301   of the ducting layer to the top and is expressed in km (Fig. 5b). Ducting thickness (Δh) for MAGIC

302   shows a near constant value of 110 m across the entire transect with only a slight increase to 130

303   m at −122.5˚, consistent with Ao et al. (2003). Conversely, the ERA5 shows a constant but slightly

304   thicker ducting layer to the east of −137.5˚ and then a decreasing thickness to the west of −137.5˚

305   (Fig. 5b).

306   The ducting layer strength is the decrease in refractivity from the bottom of the ducting layer to

307   the top (Fig. 5c) and the ratio $\Delta N/\Delta h$ reflects the average gradient of the ducting layer (Fig. 5d).

308   The ducting strength (ΔN) for the radiosondes generally ranges from 25 N-units near Hawaii to 40

309   N-units near the coast of California. Both ΔN and $\Delta N/\Delta h$ show an overall westward decreasing

310   trend along the transect which is consistent with the decrease in magnitude of the refractivity

311   gradient (Fig. 4b). Note that MAGIC and ERA5 show similar ducting strength in the eastern part

312   of the region but diverge near −137.5˚ with ERA5 10 to 20 N-units weaker than the MAGIC

313   profiles. On the other hand, ERA5 shows a ~~systematic~~systematically lower average refractivity

314   gradient ($\Delta N/\Delta h$) than MAGIC throughout the transect, indicating the challenge in ERA5 to

315   consistently resolve the sharp vertical structure in refractivity, and likewise in temperature and

316   moisture profiles, across such a thin ducting layer. The problem becomes acutely clear near the

317   trade cumulus region.
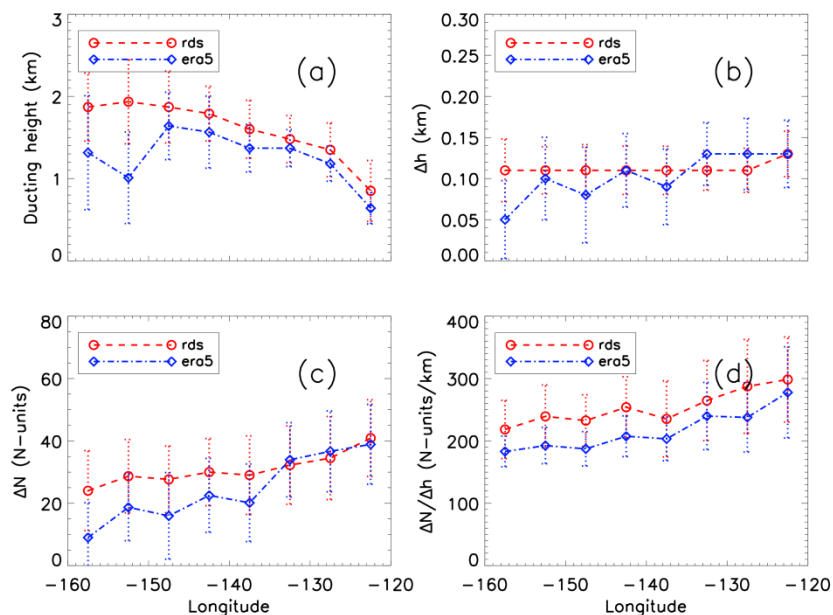
318

12

Figure 6 shows ducting layer thickness as a function of ducting layer strength, with each data point colored by its respective longitude bin. The relationship between Δh and ΔN is not longitude-dependent for either data set, but a linear trend is evident for thinner ducting layers ($\Delta h < 0.1$ km) with weaker ducting strength ($\Delta N < {\sim}25$ N-units). However, for the ducting layers thicker than 0.1 km, such a trend becomes less identifiable, and the ducting strength ΔN begins to show more variability toward larger values.
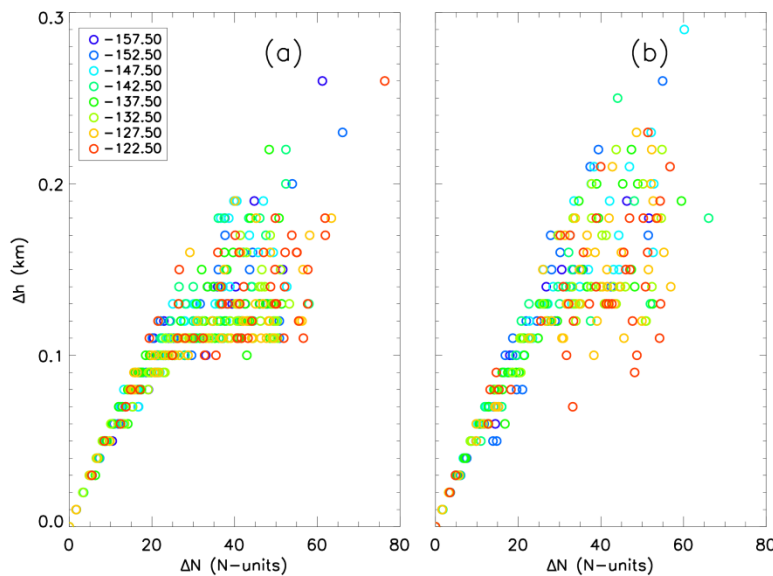
Figure 6: Comparison of individual profiles' ducting strength (ΔN) vs. ducting thickness (Δh) for MAGIC (a) and ERA5 (b). The color of each circle represents the location of the 5° longitude bin of each observation.

3.3 Ducting-induced GNSS RO *N*-bias statistics

To estimate the systematic negative *N*-bias in GNSS RO observations due to ducting, we have applied the end-to-end simulation described in ~~sect~~Sect. 2.4 to all radiosonde and ERA5 refractivity profiles with at least one elevated ducting layer detected. The *N*-bias along the transect as well as its relationship to the ducting properties are presented below.

3.3.1 Assessing ducting-induced *N*-bias

Figure 7 shows a composite of both MAGIC (396 profiles) and ERA5 (319 profiles) *N*-bias profiles which have been ~~normalized to their~~displayed as a function of an adjusted height, which is the

13

341 <u>height minus the derived</u> PBLH, with the median *N*-bias and MAD overlaid. The systematic

342 negative *N*-bias peaks at approximately 100 m below the PBLH and decreases at lower altitude.

343 The peak median value of the *N*-bias for radiosondes is −5.42% (MAD, 2.92%), nearly twice the

344 ERA5 value of −2.96% (MAD, 2.59%), indicating the significant underestimation of ducting

345 strength in ERA5 data. However, the variabilities (MAD) of the radiosonde and ERA5 data are

346 within 0.33% of each other, indicating that ERA5 data successfully capture the variations of

347 ducting features seen in the radiosondes. It is worth noting that many radiosonde profiles show

348 small negative *N*-biases above the PBLH (i.e., zero-adjusted height), which is the result of a

349 secondary ducting layer above the major ducting layer near the PBLH. ~~Conversely, few~~<u>Few</u> ERA5

350 profiles show the presence of the secondary ducting layer above PBLH.

351
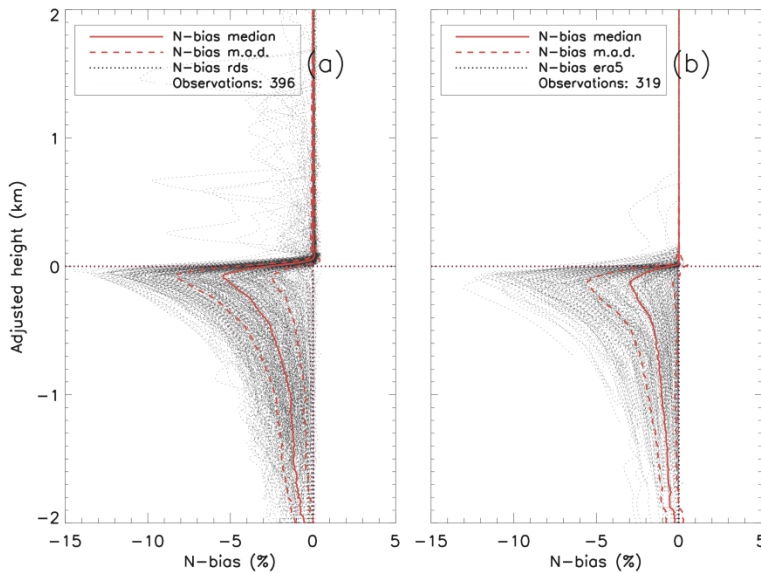
352
353 **Figure 7: Fractional refractivity difference (*N*-bias in %) between the simulated Abel-retrieved refractivity profile and the**
354 **original observation profile** ~~((N_{Abel}−N_{Obs})/N_{Obs}),~~ **for all individual observations (dotted gray): (a) MAGIC radiosondes (396**
355 **total profiles) and (b) ERA5 (319 total profiles) with population median (solid red) ± MAD (dashed red). Note the zero value**
356 **in the adjusted height refers to the PBLH for each individual *N*-bias profile.**

357 **3.3.2 Zonal variation of the *N*-bias along the transect**

358 To illustrate the large variation in the *N*-bias vertical structure resulting from the spatial variations

359 of ducting height and strength, Fig. 8 presents the *N*-bias profiles (median ± MAD) for each 5˚ bin,

360 replacing the zero adjusted height with the median PBLH for each bin. The radiosonde composite

361 (Fig. 8a) illustrates the westward transition of the median *N*-bias profiles from the largest peak *N*-

362 bias at ~0.8 km near the coast of Los Angeles, California, to a much reduced peak *N*-bias but

363   higher altitude of ~1.8 km at Honolulu, Hawaii. Table 1 lists detailed statistics of the peak *N*-bias

364   values at each bin for both radiosonde and ERA5 data. Although the vertical structure of the *N*-

365   bias profiles along the transect are consistent as seen in Fig. 7, significant changes of the *N*-bias

366   magnitude and its peak ~~*N*-bias occurring~~ height along the transect are ~~clearly~~ seen.

367   The maximum peak *N*-bias (−7.86%) in the radiosonde data is located at the easternmost of the

368   transect near California (−122.~~5°E). Whereas~~5°), whereas the minimum peak *N*-bias (−4.37%) is

369   located near the center of the transect (−147.~~5°E~~5°). Similarly, the ERA5 also show the maximum

370   peak *N*-bias (−5.92%) near California (−122.~~5°E~~5°). However, the minimum peak *N*-bias (−0.77%)

371   is found near Hawaii (−157.~~5°E~~5°). Overall, the *N*-bias ~~in~~values for the ERA5 data set are

372   ~~smaller~~less than the *N*-bias values calculated from the radiosonde ~~in all bins~~data set for each

373   longitude bin. However, a noticeable difference exists between the ERA5 and radiosonde profiles

374   for the two westernmost longitude bins (−157.~~5°E~~5° and −152.~~5°E~~5°) where the ERA5 reveals a

375   much lower and weaker *N*-bias than the MAGIC data.

376   ~~Note that the~~The PBLH is above the height of the peak *N*-bias~~, with~~ for both data sets. The MAGIC

377   data shows a maximum difference of 100 m (−137.~~5°E~~5°) and a minimum difference of ~15 m

378   (−152.~~5°E). Comparatively,~~5°) while the ERA5 ~~PBL height~~PBLH shows greater ~~difference than~~

379   ~~the height of peak *N*-bias with a~~values for maximum difference ~~of~~ (230 m ~~(~~at −142.~~5°E~~5°) and ~~a~~

380   minimum of ~~~~(45 m ~~(~~at −157.~~5°E~~5°).

381
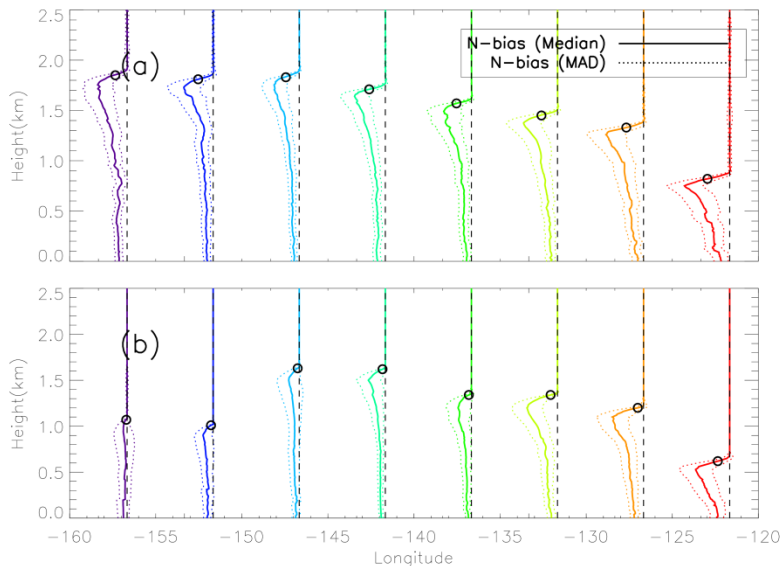
382
383   **Figure 8: Median *N*-bias (solid) ± MAD (dotted) along the north Pacific transect for MAGIC radiosondes (a) and ERA5**
384   **(b). Open circles represent the median PBLH for each 5° bin.**
385

386 **Table 1: Median and MAD peak *N*-bias (%) values for MAGIC radiosondes (RDS) and ERA5 for each 5° bin.**

Peak N-bias				
Longitude	**RDS median**	**RDS MAD**	**ERA5 median**	**ERA5 MAD**
−157.5°	−5.12	±2.61	−0.77	±1.73
−152.5°	−5.10	±2.97	−1.76	±1.61
~~−147.5°~~	~~−4.37~~	~~±2.14~~	~~−1.83~~	~~±2.10~~
−142.5°	−5.36	±2.53	−2.95	±2.17
−137.5°	−4.82	±2.96	−2.31	±2.14
−132.5°	−5.90	±3.03	−5.31	±2.68
−127.5°	−6.55	±3.40	−5.45	±2.88
−122.5°	−7.86	±3.15	−5.92	±3.04

387

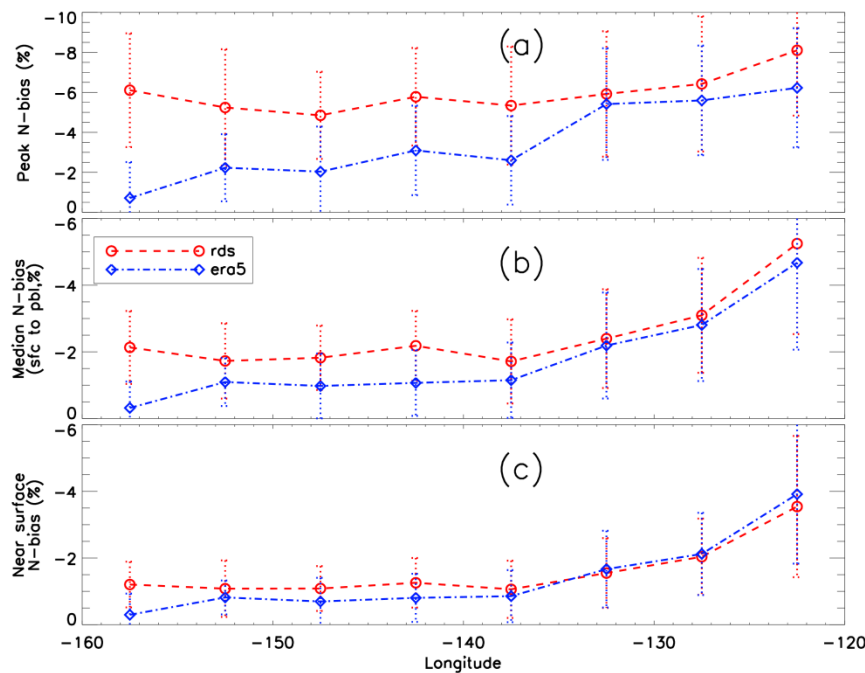| Peak N-bias (%)				
Longitude	**RDS median**	**RDS MAD**	**ERA5 median**	**ERA5 MAD**
−157.5°	−5.12	±2.61	−0.77	±1.73
−152.5°	−5.10	±2.97	−1.76	±1.61
−147.5°	−4.37	±2.14	−1.83	±2.10
−142.5°	−5.36	±2.53	−2.95	±2.17
−137.5°	−4.82	±2.96	−2.31	±2.14
−132.5°	−5.90	±3.03	−5.31	±2.68
−127.5°	−6.55	±3.40	−5.45	±2.88
−122.5°	−7.86	±3.15	−5.92	±3.04

388
389
390 Figure 9 further illustrates the peak *N*-bias, median PBL *N*-bias (0.3 km to PBLH), and the near
391 surface *N*-bias (at 0.3 km) at each bin along the transect. Note the median PBL *N*-bias refer to the
392 median value from the near surface (0.3 km) to the PBLH. Contrary to the general trend of
393 westward decrease in magnitude of the minimum refractivity gradient (Fig. 4b) and ducting
394 strength (Fig. 5c), the radiosonde peak *N*-bias –shows the maximum (median: −8.10%, MAD:
395 3.26%) near California (−122.~~5°E~~5°) and the minimum (median: −4.85%, MAD: 2.18%) over the
396 transition region (−147.~~5°E~~5°) as well as a slight increase to a secondary maximum (median:
397 −6.11%, MAD: 2.85%) near Hawaii (−157.~~5°E~~5°). The median PBL *N*-bias and the near surface
398 *N*-bias also show a similar pattern. However, the median *N*-bias demonstrates a sharp decrease in
399 the eastern half of the domain from −5.25% (MAD: 2.71%) at −122.~~5°E~~5° to −1.71% (MAD:
400 1.26%) at −137.~~5°E~~5°, and then remains relatively constant over the western half of the domain.
401 Similarly, the near surface *N*-bias reaches a maximum magnitude of −3.54% (MAD: 2.11%),
402 sharply decreases to −1.06% (MAD: 0.85%) at −137.~~5°E~~5°, and then remains relatively constant
403 over the western half of the domain.

404   Note that normalizing each *N*-bias profile to the PBLH preserves the magnitude of the *N*-bias with

405   various heights. Therefore, the relatively large normalized *N*-bias observed near Hawaii indicates

406   more persistent ducting over the trade-cumulus boundary layer regime compared to the transition

407   region in the middle of the transect at -147.~~5°E~~5° (Fig. 8a).

408   On the other hand, the ERA5 data show a westward decrease of all three *N*-biases, systematically

409   underestimating all three as compared to the radiosondes. This is expected as the decrease of ERA5

410   vertical resolution at higher altitude leads to a weaker PBL *N*-gradient observation (Fig. 4b), and

411   thus weaker ducting and a smaller ducting-induced *N*-bias. Such underestimation of the *N*-bias in

412   the ERA5 minimizes near California where the PBLH is lowest but becomes more severe

413   westward with an increase in height, reaching a maximum magnitude *N*-bias difference near

414   Hawaii. In this case, the peak *N*-bias is merely -0.71% (MAD: 1.80%) as compared to -6.23%

415   (MAD: 2.98%) at $-122.$~~5°E~~5° (Fig. 9a ~~and Table 1~~). The large difference seen in the *N*-bias along

416   the transect strongly indicates the challenges of the ERA5 data to resolve the sharp gradient across

417   the ducting layer, resulting in a large variation in PBLH of the ERA5 data in the western segment

418   of the region. The increasing difference between the radiosonde and ERA5 data from east to west

419   is most pronounced in the peak *N*-bias cross-section (Fig. 9a) but is also evident in both the median

420   *N*-bias (Fig. 9b) as well as the near surface *N*-bias (Fig. 9c).

421
422   **Figure 9: Zonal transect of 5° bin (a) peak *N*-bias, (b) median PBL *N*-bias (0.3 km to PBLH), and (c) near surface *N*-bias at**
423   **0.3 km for MAGIC (median in red circle and red-dashed line, MAD in red-dotted error bar) and ERA5 (median in blue**
424   **diamond and dot-dashed line, MAD in blue-dotted error bar)**

3.3.3 The relationship between *N*-bias and key variables

Figure 10 shows a scatter plot of the PBLH vs. height of peak *N*-bias along the transect with each data point colored by the center longitude of the bin to which it belongs. The PBLH and the height of peak *N*-bias show a clear linear relationship with high correlation for both the MAGIC (0.89) and ERA5 (0.98) data. The majority of the radiosonde data show the heights of peak *N*-bias align well with the PBLH with a very small low bias (less than 80 m). The reason for the lower correlation value in MAGIC data is attributed to outlier cases when the radiosonde *N*-bias profiles with a double peak at which the larger magnitude bias is located (Fig. 7a). On the other hand, the ERA5 maximum ducting heights show little difference from the PBLH near California (e.g., =122.5°E), but become lower moving westward, which is illustrated by the increasing difference between the linear regression line and the 1:1 line.
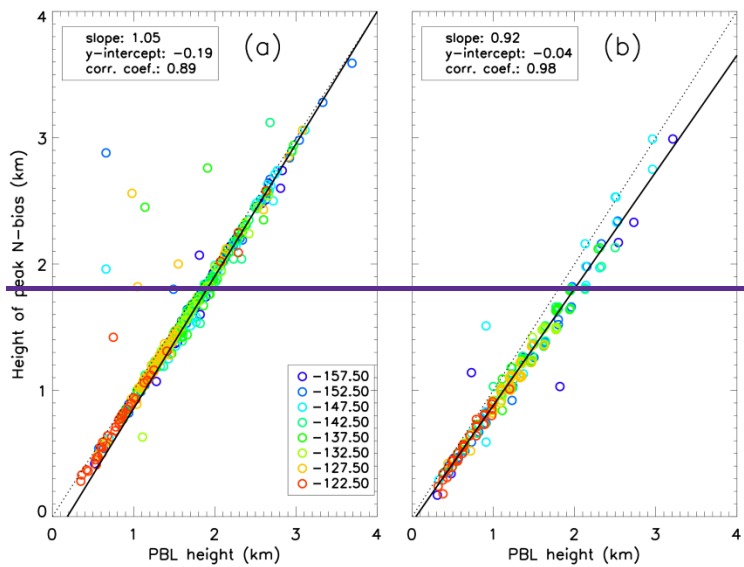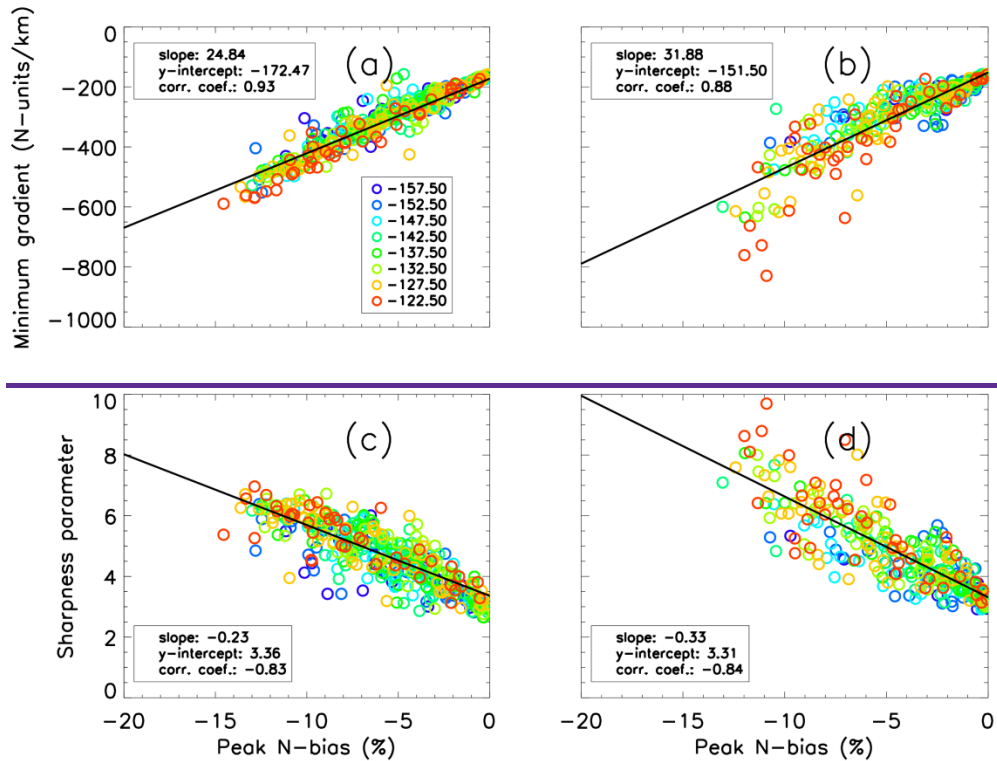

Figure 10: PBLH vs. height of peak *N*-bias for individual profiles from MAGIC (a) and ERA5 (b) data. The color of each open circle represents the center longitude of the 5° bin to which each profile belongs.

Figure 11 shows a near-linear relationship between the minimum refractivity gradients and the peak *N*-biases for both MAGIC radiosondes and ERA5 profiles, i.e., the sharper the refractivity gradient, the larger the *N*-bias. The correlation coefficient for both MAGIC radiosondes (0.93) and the ERA5 profiles (0.88) are also presented. The sharpness parameter (Fig. 11c, 11d) also shows a linear relationship with the maximum *N*-bias which is a result of its dependence on the minimum refractivity gradient. Interestingly, their relationship with the peak *N*-bias exhibits no indication of zonal dependence.

4   Summary and Conclusions

In this study, radiosonde profiles from the MAGIC field campaign have been analyzed to investigate ducting characteristics and the induced systematic refractivity biases in GNSS RO retrievals over the Northeastern Pacific Ocean between Hawaii and California. Colocated ERA5 model reanalysis data were used as a secondary comparison to the radiosonde observations.

The nearly 1-year high-resolution MAGIC radiosonde ~~dataset~~data set reveals the frequent presence of ducting marked by a sharp refractivity gradient resulting from the large moisture lapse rate across a strong temperature inversion layer. The PBLH increases by more than 1 km along the transect from California to Hawaii while the magnitude of the refractivity gradient decreases by 100 N-units km^{-1}. The zonal gradient of both variables illustrates the transition of the PBL from shallow stratocumulus adjacent to the California coast to deeper trade-wind cumulus that are prevalent near the Hawaiian Islands.

End-to-end simulation on all radiosonde and ERA5 refractivity profiles has been conducted to estimate the systematic negative N-bias in GNSS RO observations. The ducting layer maintains

466   remarkably consistent thickness ((~110 m) along the transect with westward decreasing strength

467   and increasing height. The ERA5 slightly underestimates both the height and strength of the

468   ducting layer as well as the PBLH. A systematic negative ~~refractivity bias (~~N-bias~~)~~ below the

469   ducting layer is observed throughout the transect, peaking (−5.42%) approximately 80 meters

470   below the ~~PBL height~~PBLH, and gradually decreasing towards the surface (−0.5%). ~~The height of~~

471   ~~the peak N-bias and the PBLH show a highly positive correlation. The median difference between~~

472   ~~the two is about 80 meters in the radiosonde but increasing to about 120 meters in the colocated~~

473   ~~ERA5 data.~~

474   MAGIC radiosondes indicate larger values of both ducting strength (ΔN) and thickness (Δh) than

475   ERA5 in the western half of the transect. The opposite is true in the eastern portion of the domain,

476   and is likely associated with the transition of the cloud layer from open-cell cumulus in the west

477   to stratocumulus and stratus in the east (Wood et al., 2011; Bretherton et al., 2019~~; Wood et al.,~~

478   ~~2011). The~~). ERA5 systematically underestimates the average ducting layer gradient ($\Delta N/\Delta h$)

479   comparing to the radiosondes. The largest N-bias is found over the region with strongest ducting

480   and largest sharpness parameter. It is worth noting that the PBL over the western portion of the

481   transect near Hawaii frequently shows two major gradient layers (a mixing layer at ~1 km and the

482   trade-inversion at ~2 km), with comparable N-gradients (e.g., Fig. 2). The much lower PBLH seen

483   in ERA5 in this region is likely due, in part, to the decreasing number of model levels in ERA5 at

484   higher altitude, which could lead to higher possibility of identifying the lower gradient layer as the

485   PBLH. However, the impact of the vertical resolution on the performance of gradient method for

486   PBLH detection has not been performed in this study and warrants more comprehensive study in

487   the future.

488

489

490

491

492

493

494

495

496

5 Data availability

Data for the Marine Atmospheric Radiation Measurement (ARM) GCSS Pacific Cross Section Intercomparison (GPCI) Investigation of Clouds (MAGIC, Zhou et al., 2015) can be accessed through the U.S. Department of Energy's Office of Science https://www.arm.gov/research/campaigns/amf2012magic.

Data for the ECMWF Reanalysis version 5 (ERA5, Hersbach et al., 2020) can be accessed at https://www.ecmwf.int/en/forecasts/dataset/ecmwf-reanalysis-v5.

6 Author contribution

Author Thomas Winning is responsible for all original text and, data analysis and production of graphics. Author Kevin Nelson contributed by providing updated data processing code, colocation of ERA5 data with MAGIC observations and first and second round edits. Author Feiqin Xie is the academic advisor for the primary author and also provided draft edits and paper organization and writing guidance.

7 Competing interests

The authors declare no competing interests, see Acknowledgements for current affiliationaffiliations.

8 Acknowledgements

529   **References**

530   Anthes, R. A., and Coauthors: The COSMIC/FORMOSAT-3 Mission: Early Results, BAMS, 89, 313–334,

531   doi.org/10.1175/bams-89-3-313, 2008.

532

533   Ao, C. O., Meehan T. K., Hajj, G. A., Mannucci, A. J., and Beyerle, G.: Lower Troposphere Refractivity Bias in GPS

534   Occultation Retrievals, J. Geophys. Res., 108, 4577, doi:10.1029/2002JD003216, 2003.

535

536   Ao, C. O.: Effect of Ducting on Radio Occultation Measurements: An Assessment Based on High-resolution

537   Radiosonde Soundings, Radio Sci., 42, RS2008, doi.org/10.1029/2006RS003485, 2007.

538

539   Ao, C. O., Chan, T. K., Iijima, A., Li, J.-L., Mannucci, A. J., Teixeira, J., Tian, B., and Waliser, D. E.: Planetary

540   Boundary Layer Information from GPS Radio Occultation Measurements, in: Proceedings of the GRAS SAF

541   Workshop on Applications of GPSRO Measurements, Vol. 5 of, GRAS SAF Workshop on Applications of GPSRO

542   Measurements, Reading, United Kingdom, ECMWF and EUMETSAT, 123–131,

543   https://www.ecmwf.int/sites/default/files/elibrary/2008/7459-planetary-boundary-layer-information-gps-radio-

544   occultation-measurements.pdf, 16–18 June, 2008.

545

546   Ao, C. O., Waliser, D. E., Chan, S. K., Li, J.-L., Tian, B., Xie, F., and Mannucci, A. J.: Planetary boundary layer

547   heights from GPS radio occultation refractivity and humidity profiles, J. Geophys. Res., 117, D16117,

548   doi:10.1029/2012JD017598, 2012.

549

550   Basha, G., and Ratnam, M. V.: Identification of atmospheric boundary layer height over a tropical station using high-

551   resolution radiosonde refractivity profiles: Comparison with GPS radio occultation measurements, J. Geophys. Res.,

552   114, doi.org/10.1029/2008jd011692, 2009.

553

554   Beyerle, G., Gorbunov, M. E., and Ao, C.O.: Simulation studies of GPS radio occultation measurements, Radio Sci.,

555   38, 1084, doi:10.1029/2002RS002800, 2003.

556

557   Bretherton, C.S., and Coauthors: Cloud, Aerosol, and Boundary Layer Structure across the Northeast Pacific

558   Stratocumulus–Cumulus Transition as Observed during CSET, Mon.Wea. Rev., 147, 2083–2102. DOI:

559   10.1175/MWR-D-18-0281, 2019

560

561 Eshleman, V.R.: The radio occultation method for the study of planetary atmospheres, Planet. Space Sci., 21, 1521-
562 1531, doi.org/10.1016/0032-0633(73)90059-7, 1973.

563

564 Feng, X., Xie, F., Ao, C.O., and Anthes, R.A.: Ducting and Biases of GPS Radio Occultation Bending Angle and
565 Refractivity in the Moist Lower Troposphere, J. Atmos. Oceanic Technol., 37, 1013–1025, doi.org/10.1175/JTECH-
566 D-19-0206.1, 2020.

567

568 Fjeldbo, G., and Eshleman, V.R.: The Atmosphere of Mars Analyzed by Integral Inversion of the Mariner IV
569 Occultation Data, Planet. Space Sci., 16, 1035-1059, doi.org/10.1016/0032-0633(68)90020-2, 1968.

570

571 Fjeldbo, G., Kliore, A.J., and Eshleman, V.R.: The Neutral Atmosphere of Venus as Studied with the Mariner V Radio
572 Occultation Experiment, Astron. J., 76, 123-140, doi.org/10.1086/111096, 1971.

573

574 Garratt, J. R.: Review: the atmospheric boundary layer, Earth-Sci. Rev., 37, 89–134, 1994

575

576 Guo, P., Kuo, Y. H., Sokolovskiy, S. V., and Lenschow, D. H.: Estimating Atmospheric Boundary Layer Depth Using
577 COSMIC Radio Occultation Data, J. Atmos. Sci., 68, 1703–1713, doi.org/10.1175/2011jas3612.1, 2011.

578

579 Gorbunov, M. E.: Canonical transform method for processing radio occultation data in the lower troposphere, Radio
580 Sci., 37(5), 1076, doi:10.1029/2000RS002592, 2002.

581
582 Gorbunov, M. E., Benzon, H. H., Jensen, A.S, Lohmann, M.S., and Nielsen, A.S.: Comparative analysis of radio
583 occultation processing approaches based on Fourier integral operators. Radio Sci., 39, RS6004,
584 https://doi.org/10.1029/2003RS002916, 2004

585

586 Healy, S. B.: Radio occultation bending angle and impact parameter errors caused by horizontal refractive index
587 gradients in the troposphere: A simulation study, J. Geophys. Res, 106, D11, 11875–11889,
588 doi:10.1029/2001JD900050, 2001.

589

590 Hersbach, H., Bell, B., Berrisford, P., Hirahara, S., Horányi, A., Muñoz-Sabater, J., Nicolas, J., Peubey, C., Radu, R.,
591 Schepers, D., Simmons, A., Soci, C., Abdalla, S., Abellan, X., Balsamo, G., Bechtold, P., Biavati, G., Bidlot, J.,
592 Bonavita, M., De Chiara, G., Dahlgren, P., Dee, D., Diamantakis, M., Dragani, R., Flemming, J., Forbes, R., Fuentes,
593 M., Geer, A., Haimberger, L., Healy, S., Hogan, R. J., Hólm, E., Janisková, M., Keeley, S.,
594 Laloyaux, P., Lopez, P., Lupu, C., Radnoti, G., de Rosnay, P., Rozum, I., Vamborg, F., Villaume, S., and Thépaut, J.-
595 N.: The ERA5 Global Reanalysis, Q. J. Roy. Meteor. Soc., 146, 1999–2049, https://doi.org/10.1002/qj.3803, 2020.

596

597   Ho, S.-P., Peng, L., Anthes, R. A., Kuo, Y.-H., and Lin, H.-C.: Marine boundary layer heights and their longitudinal,

598   diurnal and inter-seasonal variability in the southeast Pacific using COSMIC, CALIOP, and radiosonde data. J.

599   Climate, 28, 2856–2872, https://doi.org/10.1175/JCLI-D-14-00238.1, 2015.

600

601   Jensen, A. S., Lohmann, M.S., Nielsen, A.S. and Benzon, H.-H.: Geometrical optics phase matching of radio

602   occultation signals, Radio Sci., 39, RS3009, doi:10.1029/2003RS002899, 2004.

603

604   Jensen, A. S., Lohmann, M.S., Benzon, H.-H, and Nielsen, A.S.: Full spectrum inversion of radio occultation signals,

605   Radio Sci., 38(3), 1040, doi:10.1029/2002RS002763, 2003.

606

607   Johnston, B. R., Xie, F., and Liu, C.: The effects of deep convection on regional temperature structure in the tropical

608   upper troposphere and lower stratosphere, J. Geophys. Res.: Atmos., 123, 1585−1603,

609   doi.org/10.1002/2017JD027120, 2018.

610

611   Klein, S. A., and Hartmann, D. L.: The seasonal cycle of low stratiform clouds. Journal of Climate, 6, 1587−1606,

612   doi:~~10.1175/1520-0442(1993)006<1587:TSCOLS>2.0.CO;2~~10.1175/1520-

613   0442(1993)006<1587:TSCOLS>2.0.CO;2, 1993.

614

615   Kursinski, E. R., Hajj, G. A., Schofield, J. T., Linfield, R. P., and Hardy, K. R.: Observing Earth's atmosphere with

616   radio occultation measurements using the Global Positioning System, J. Geophys. Res.: Atmos., 102, 23429−23465,

617   doi.org/10.1029/97jd01569, 1997.

618

619   Kursinski, E. R., G. A. Hajj, Leroy, S. S., and Herman, B.: The GPS Radio Occultation Technique. Terr. Atmos.

620   Ocean. Sci. (TAO), 11, 53−114, 2000.

621

622   Lewis, E. R.: Marine ARM GPCI Investigation of Clouds (MAGIC) Field Campaign Report. U.S. Department of

623   Energy, https://doi.org/10.2172/1343577, 2016.

624

625   Maddy, E. S. and Barnet, C. D.: Vertical resolution estimates in version 5 of AIRS operational retrievals. IEEE

626   Transactions on Geoscience and Remote Sensing, 46, 2375−2384,

627   doi:~~10.1109/TGRS.2008.91749~~810.1109/TGRS.2008.917498, 2008.

628

629   Nelson, K. J., Xie, F., Ao, C. O., and Oyola-Merced, M. I.: Diurnal Variation of the Planetary Boundary Layer Height

630   Observed from GNSS Radio Occultation and Radiosonde Soundings over the Southern Great Plains. J. Atmos.

631   Oceanic Tech., 38, 2081−2093, https://doi.org/10.1175/jtech-d-20-0196.1, 2021.

632

633 Nelson, K. J., Xie, F., Chan, B. C., Goel, A., Kosh, J., Reid, T. G. R., Snyder, C. R., and Tarantino, P. M.: GNSS
634 Radio Occultation Soundings from Commercial Off-the-Shelf Receivers Onboard Balloon Platforms, Atmos. Meas.
635 Tech., https://doi.org/10.5194/amt-2022-198, 2022.

636

637 Painemal, D., Minnis, P., and Nordeen, M.: Aerosol variability, synoptic-scale processes, and their link to the cloud
638 microphysics over the northeast Pacific during MAGIC, J. Geophys. Res. Atmos., 120, 5122–5139,
639 doi:10.1002/2015JD023175, 2015.

640

641 Patterson, W. L.: Climatology of Marine Atmospheric Refractive Effects: A Compendium of the Integrated Refractive
642 Effects Prediction System (IREPS) Historical Summaries. Naval Ocean Systems Center,
643 https://apps.dtic.mil/sti/pdfs/ADA155241.pdf, 1982.

644

645 Ramanathan, V., Cess, R. D., Harrison, E. F., Minnis, P., Barkstrom, B. R., Ahmad, E., and Hartmann, D.: Cloud-
646 radiative forcing and climate: Results from the Earth Radiation Budget Experiment, Science, 243, 57–63,
647 DOI:~~10.1126/science.243.4887.57~~10.1126/science.243.4887.57, 1989.

648

649 Riehl, H.: Climate and weather in the tropics. London: Academic Press. 611 pp. ISBN 0.12.588180.0

650

651 Rocken, C., Anthes, R., Exner, M., Hunt, D., Sokolovskiy, S., Ware, R., Gorbunov, M., Schreiner, W., Feng
652 D., Herman B., Kuo, Y.-H., Zou, X.: Analysis and validation of GPS/MET data in the neutral atmosphere. J. Geophys.
653 Res., 102, 29849−29866, https://doi.org/10.1029/97JD02400, 1997.

654

655 Schreiner, W. S., Weiss, J.P., Anthes, R.A., Braun, J., Chu, V., Fong, J., Hunt, D., Kuo, Y.-H., Meehan, T., Serafino,
656 W., Sjoberg, J., Sokolovskiy, C., Talaat, E., Wee, T.K., Zeng, Z.: COSMIC-2 Radio Occultation Constellation: First
657 Results. Geophys. Res. Lett., 47, https://doi.org/10.1029/2019gl086841, 2020.

658

659 Seidel, D. J., Ao, C.O. and Li, K.: Estimating climatological planetary boundary layer heights from radiosonde
660 observations: Comparison of methods and uncertainty analysis, J. Geophys. Res., 115, D16114,
661 doi:10.1029/2009JD013680, 2010.

662

663 Smith, E. K. and Weintraub, S.: The Constants in the Equation for Atmospheric Refractivity Index at Radio
664 Frequencies. Proc. IRE, 41, 1035−1037, doi:~~10.1109/JRPROC.1953.274297~~10.1109/JRPROC.1953.274297, 1953.

665

666 Sokolovskiy, S. V.: Modeling and Inverting Radio Occultation Signals in the Moist Troposphere. Radio Sci., 36,
667 441−458, https://doi.org/10.1029/1999RS002273, 2001.

668

669 Sokolovskiy, S. V.: Effect of super refraction on inversions of radio occultation signals in the lower troposphere.
670 Radio Sci., 38 (3), https://doi.org/10.1029/2002RS002728, 2003.

671

672 Sokolovskiy, S. V., Kuo, Y.-H., Rocken, C., Schreiner, W. S., Hunt, D. and Anthes, R. A., 2006: Monitoring the
673 atmospheric boundary layer by GPS radio occultation signals recorded in the open-loop mode. Geophys. Res. Lett.,
674 33, L12813, doi:10.1029/2006GL025955, 2006.

675

676 Stull, R., Santoso, E., Berg, L. K., and Hacker, J.: Boundary Layer Experiment 1996 (BLX96), BAMS, 78,
677 1149−1158, doi: 10.1175/1520-0477(1997)078<1149:BLEB>2.0.CO;2, 1997.

678

679 Stull, R. B.: An Introduction to Boundary Layer Meteorology. Kluwer Academic Publishers, 666 pp., ISBN 90-277-
680 2768-6, 1988.

681

682 von Engeln, A. and Teixeira, J.: A Planetary Boundary Layer Height Climatology Derived from ECMWF Reanalysis
683 Data, J. Climate, 26, 6575−6590, https://doi.org/10.1175/jcli-d-12-00385.1, 2013.

684

685 Winning, T. E., Chen, Y.-L., and Xie, F.: Estimation of the marine boundary layer height over the central North Pacific
686 using GPS radio occultation, Atmospheric Research, 183, 362−370, https://doi.org/10.1016/j.atmosres.2016.08.005,
687 2017.

688

689 Wood, R., Mechoso, C. R., Bretherton, C. S., Weller, R. A., Huebert, B., Straneo, F., Albrecht, B. A., Coe, H., Allen,
690 G., Vaughan, G., Daum, P., Fairall, C., Chand, D., Gallardo Klenner, L., Garreaud, R., Grados, C., Covert, D. S.,
691 Bates, T. S., Krejci, R., Russell, L. M., de Szoeke, S., Brewer, A., Yuter, S. E., Springston, S. R., Chaigneau, A.,
692 Toniazzo, T., Minnis, P., Palikonda, R., Abel, S. J., Brown, W. O. J., Williams, S., Fochesatto, J., Brioude, J., and
693 Bower, K. N.: The VAMOS Ocean-Cloud-Atmosphere-Land Study Regional Experiment (VOCALS-REx): goals,
694 platforms, and field operations, Atmos. Chem. Phys., 11, 627−654, https://doi.org/10.5194/acp-11-627-2011, 2011.

695

696 Xie, F., Syndergaard, S., Kursinski, E. R., and Herman, B.M.: An Approach for Retrieving Marine Boundary Layer
697 Refractivity from GPS Occultation Data in the Presence of Super-refraction. J. Atmos. Oceanic Technol., 23,
698 1629−1644, https://doi.org/10.1175/JTECH1996.1, 2006.

699

700 Xie, F., Haase, J. S., and Syndergaard, S.: Profiling the Atmosphere Using the Airborne GPS Radio Occultation
701 Technique: A Sensitivity Study. IEEE Transactions on Geoscience and Remote Sensing, 46, 3424−3435,
702 https://doi.org/10.1109/tgrs.2008.2004713, 2008.

703

704 Xie, F., Wu, D. L., Ao, C. O., Kursinski, E. R., Mannucci, A. J., and Syndergaard, S.: Super-refraction effects on GPS
705 radio occultation refractivity in marine boundary layers, Geophys. Res. Lett., 37,
706 https://doi.org/10.1029/2010gl043299, 2010.

707

708 Xie, F., Wu, D. L., Ao, C. O., Mannucci, A. J., and Kursinski, E. R.: Advances and limitations of atmospheric boundary
709 layer observations with GPS occultation over southeast Pacific Ocean, Atmos. Chem. Phys., 12, 903−918,
710 doi:10.5194/acp-12-903-2012, 2012.

711

712 Zhou, X., Kollias, P., and Lewis, E.: Clouds, precipitation and marine boundary layer structure during MAGIC. J.
713 Climate, 28, 2420−2442, https://doi.org/10.1175/JCLI-D-14-00320.1, 2015.